




**Position-dependent plasmonic chirality of particles in tightly focused light field**Guodong Zhu,<sup>1</sup> Zhiguang Sun,<sup>1,2</sup> Shuo Zhang,<sup>1</sup> Haoran Liu<sup>1</sup>,, Yongqi Chen,<sup>1</sup> Nan Gao<sup>1</sup>,  
Wei Peng,<sup>1</sup> and Yurui Fang<sup>1,\*</sup><sup>1</sup>*School of Physics, Dalian University of Technology, Dalian 116024, People's Republic of China*<sup>2</sup>*Instrumental Analysis Center, Dalian University of Technology, Dalian 116024, People's Republic of China*

(Received 29 February 2024; accepted 10 July 2024; published 5 August 2024)

Plasmonic chirality garners considerable attention owing to its distinctive optical characteristics and wide-ranging applications. Understanding the optical activity of single particles holds paramount significance for both theoretical frameworks and experimental measurements of chirality. When probing the optical response of chiral particles, high numerical aperture (NA) objectives, adept at concentrating light into exceedingly small regions, are frequently employed. With escalating NA, the incident light no longer satisfies the paraxial approximation, engendering electric field components perpendicular to the focal plane. However, this electric field component is usually neglected in research. Here, we utilize angular spectrum theory to explore the optical response and circular dichroism of single chiral nanoparticles subjected to tightly focused circularly polarized light. Remarkably, we find that the electric field component perpendicular to the focal plane exhibits a pronounced influence on chirality, potentially inducing a reversed circular dichroism response when the particle deviates from the optical axis. Simultaneously, variations in the position of particles within the light field yield significant discrepancies in higher-order modes, particularly electric quadrupole moments. Our findings hold profound implications for the measurement and analysis of chiral particles, offering invaluable guidance for the future investigations of chirality.

DOI: [10.1103/PhysRevA.110.023506](https://doi.org/10.1103/PhysRevA.110.023506)**I. INTRODUCTION**

Optical chirality, the phenomenon where objects exhibit disparate behaviors under left-circularly polarized light versus right-circularly polarized light, has garnered considerable attention owing to its widespread occurrence in nature [1]. The interaction of light with chiral molecules engenders captivating optical phenomena such as optical rotation and circular dichroism. However, natural chiral molecules typically manifest exceedingly weak chiral responses, predominantly confined to the ultraviolet spectrum, thereby constraining accuracy of their detection. Recent advancements in nanofabrication technology have spurred intense interest in plasmonic chirality, owing to its tunability over the optical spectral range and great circular dichroism (CD). Numerous chiral metamolecules have been proposed and demonstrated to have chiral optical responses [2–5], which can be applied to manipulate the polarization state of light [6–8], detect chiral molecules [9–15] based on superchiral fields [16,17], diagnose diseases [18,19], and other applications [20,21].

Accurate measurement and analysis of chiral metamolecules are imperative for realizing practical applications of plasmonic chirality. The exploration of a single chiral particle can reduce the deviation of measured results caused by the average effect and the inhomogeneity of large-area samples [22–24]. Consequently, exploring single particles is crucial to elucidating the intrinsic mechanism of chirality,

thereby facilitating the optimization of chiral metamaterial design. When the particle size is larger than  $1/20$  of the wavelength, the scattering effect has a non-negligible impact on the CD response, showing obvious circular differential scattering [25]. Therefore, single-particle spectroscopy techniques such as dark-field microscopy, and supercontinuum white light confocal microscopy [26], are widely used in single-particle chirality measurements. In the above-mentioned spectral measurement of a single chiral particle, it is inevitable to utilize high-NA objectives or a dark-field condenser to concentrate incident light into subwavelength regions, which naturally generates a longitudinal electric field at its focus [27–29]. Although this electric field component is small, it can still have a discernible effect on the chiral signal when the nanoparticle is off optical axis. Simultaneously, the light field focused by the objective lens or condenser can exhibit elliptical polarization off axis; the linear dichroism artifacts caused by the above phenomenon are also of concern to researchers [30,31]. Moreover, the particles cannot always be guaranteed to be exactly in the optical axis of the focus spot in optical experiments. Therefore, although the chirality of a single particle under weakly focused circularly polarized light has been explored [24], there is still an urgent need to explore the position-dependent chiral response of particles under tightly focused circularly polarized light.

In this paper, we investigate the chiral optical response of single plasmonic chiral particles in Fig. 1(a) excited by tightly focused circularly polarized light derived from angular spectrum theory. Due to the distinctive electric field distribution of the tightly focused light field [Fig. 1(b)], we found that when

\*Contact author: [yrfang@dlut.edu.cn](mailto:yrfang@dlut.edu.cn)

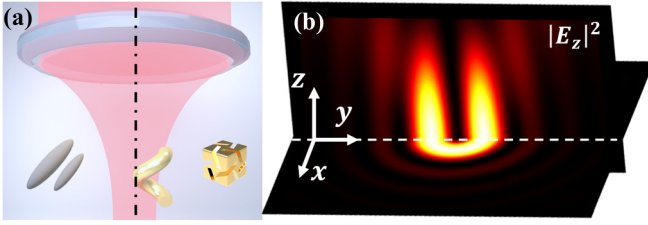


FIG. 1. Schematic diagram of a single chiral gold nanostructure excited by a tightly focused beam. (a) Chiral particles excited by the light field focused by the objective lens. (b) Annular distribution of  $z$ -component electric field intensity of tightly focused circularly polarized light.

the nanostructure is on the optical axis, its optical response closely mirrors that observed under plane-wave excitation. However, the off-axis chiral particle experiences a significant influence from the electric field component perpendicular to the focal plane, resulting in a notable difference in circular dichroism and even inducing an opposite chiral signal. To comprehensively explore this effect, a multipolar decomposition is employed to delineate the optical scattering cross section as well as the chiral signal. Experimentally, we also measured the position dependence of a single chiral nanohelicoid in a tightly focused light field, which validated our results well.

## II. THEORY AND SIMULATION

Here, we follow the method of Richards and Wolf to calculate the electric field of tightly focused light passing through a lens by the Debye integral [28,29]. Consider a circularly polarized plane wave propagating in the positive direction of the  $z$  axis incident on an aplanatic objective (reference sphere) with focal length  $f$ , where  $f$  is much larger than the incident wavelength. As shown in Fig. 2, the field  $\mathbf{E}$  near the focus  $\mathbf{O}$  is determined by the far-field  $\mathbf{E}_\infty$  on the reference sphere. The reference sphere transforms the cylindrical coordinate system (incident beam) to the spherical coordinate system (focused beam). Thus we can express the angular spectrum

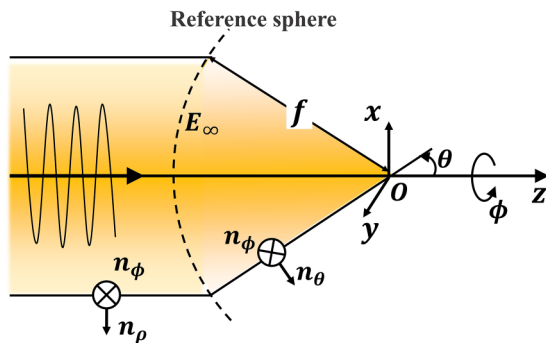


FIG. 2. Geometrical representation of incident light refracted by lens system and coordinate definition.  $\mathbf{n}_\rho$  and  $\mathbf{n}_\phi$  are the unit vectors of a cylindrical coordinate system, whereas  $\mathbf{n}_\theta$  and  $\mathbf{n}_\phi$  are the unit vectors of a spherical coordinate system.

representation of the focal field as [27]

$$\mathbf{E}(\rho, \varphi, z) = \frac{ikf}{2\pi} \int_0^{\theta_{\text{NA}}} \int_0^{2\pi} \mathbf{E}_\infty(\theta, \phi) e^{-ikz\cos\theta} \times e^{-ik\rho\sin\theta\cos(\phi-\varphi)} \sin\theta d\phi d\theta, \quad (1)$$

where  $k$  is the wave vector in the medium.  $\theta_{\text{NA}} = \arcsin(\text{NA}/n)$  represents the maximum aperture angle, and  $n$  is the refractive index of the surrounding medium.

Here, we use the time factor  $e^{i\omega t}$  to facilitate the following numerical calculations. The polarization of the incident light can be represented by a matrix,  $\mathbf{E}_{\text{inc}} = [1 \quad c_{\text{pl}} \quad 0]$ , where  $c_{\text{pl}} = \pm i$  represent different circular polarization states and  $c_{\text{pl}} = 0$  represents linearly polarized light with  $x$  polarization. For simplicity, we assume that the focusing objective lens has a good antireflection coating so that we can ignore the Fresnel transmission coefficient, then the far-field  $\mathbf{E}_\infty$  can be expressed as

$$\mathbf{E}_\infty = \frac{E_0}{2} \begin{bmatrix} (\cos\theta - 1)(\cos 2\phi + c_{\text{pl}}\sin 2\phi) + (1 + \cos\theta) \\ (\cos\theta - 1)(\sin 2\phi - c_{\text{pl}}\cos 2\phi) + c_{\text{pl}}(1 + \cos\theta) \\ -2\sin\theta\cos\phi - 2c_{\text{pl}}\sin\theta\sin\phi \end{bmatrix} \times \sqrt{\cos\theta}. \quad (2)$$

Substituting Eq. (2) into Eq. (1), we can get the Cartesian vector components of the focus field near the focal point as

$$\mathbf{E}(\rho, \varphi, z) = \begin{bmatrix} E_x \\ E_y \\ E_z \end{bmatrix} = \frac{ikf}{2} E_0 \begin{bmatrix} I_0 + I_2(\cos 2\varphi + c_{\text{pl}}\sin 2\varphi) \\ c_{\text{pl}}I_0 + I_2(\sin 2\varphi - c_{\text{pl}}\cos 2\varphi) \\ 2iI_1(\cos\varphi + c_{\text{pl}}\sin\varphi) \end{bmatrix}. \quad (3)$$

Here, we use the following integral abbreviations for convenience:

$$I_0 = \int_0^{\theta_{\text{NA}}} \sqrt{\cos\theta}(1 + \cos\theta) J_0(k\rho\sin\theta) e^{-ikz\cos\theta} \sin\theta d\theta, \quad (4a)$$

$$I_1 = \int_0^{\theta_{\text{NA}}} \sqrt{\cos\theta}\sin\theta J_1(k\rho\sin\theta) e^{-ikz\cos\theta} \sin\theta d\theta, \quad (4b)$$

$$I_2 = \int_0^{\theta_{\text{NA}}} \sqrt{\cos\theta}(1 - \cos\theta) J_2(k\rho\sin\theta) e^{-ikz\cos\theta} \sin\theta d\theta. \quad (4c)$$

Model simulations were performed with full-wave numerical simulations by using the commercial finite element method software package COMSOL. The scattering field method in COMSOL is applied to calculate the optical response of the chiral nanoparticles, and the background field is given by the formula derived from the angular spectrum. The plasmonic gold nanoparticle was placed in the air, and the dielectric functions of gold and silver were obtained from Ref. [32]. The simulations were run in the spectral range between 500 and 1500 nm with a spectral step size of 10 nm, and the parameters of the structure and simulation

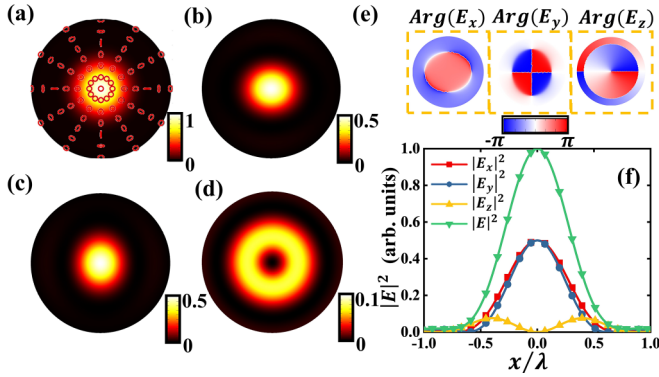


FIG. 3. Focal field distribution at plane  $z = 0$  nm for an incoming circularly polarized light of wavelength 633 nm. (a) The total energy density of the electric field; the red circles are the polarization states at different positions in the light field. (b)–(d) the  $x$ ,  $y$ , and  $z$  components of the electric energy density; all the distributions are normalized to the maximum value of  $E_{\text{total}}$ . (e) The relative phase of the electric field. (f) Normalized electric field components of tightly focused circularly polarized light.

details can be found in Appendix A. The induced polarization density was also extracted for the spectral multipolar decomposition of the investigated structures [33,34].

### III. RESULT AND DISCUSSION

Figure 3 shows the energy density of the focal field on the plane  $z = 0$  when the incident wavelength of 633 nm is focused by an air-objective lens with a NA of 0.9. The distribution of the focal field components presented here takes into account the experiment conditions, such as the wavelength of the beam, the NA of the lens, the focal length, etc. The high NA of the objective leads to highly nonparaxial propagation of the focused light field, so a full vector description is crucial. The red circle in Fig. 3(a) is the polarization state on the  $z = 0$  nm plane. It can be seen that when deviating from the focus, the polarization state of the incident circularly polarized light will be transformed into elliptically polarized light. A strong longitudinal electric field component is formed off axis as shown in Fig. 3(d); there is no longitudinal electric field at the focus, and the transverse electric field (perpendicular to the wave vector) is dominant. Since the spot radius of the focused field increases with the incident wavelength, we define an offset factor  $\kappa = x/\lambda_{\text{resonance}}$  to explore the dependence of the optical activity of chiral metamolecules on their position in the tightly focused field. Figure 3(f) shows the proportion of the energy density of each electric field component in the total energy density under different offset factors, and the energy density of the light field at a higher numerical aperture with a refractive index of 1.51 for the surrounding medium is also included in Fig. 8 of Appendix A. When  $\kappa = 0.3$ , the longitudinal energy density is maximum. When  $\kappa = 0.7$ , the total electric field energy is weak, but the longitudinal energy density is much greater than the transverse energy density.

For the numerical study, we choose gold helicoids [10,19], a gold nanohelix [8,22], and silver nanorices dimers [35,36] to explore the optical activity in the interaction of tightly focused

light fields with the chiral particles, where helicoids and the helix correspond to intrinsic chirality, and the dimer corresponds to extrinsic chirality. The nanohelix is illuminated by a tightly focused circularly polarization light beam that propagates along the positive  $z$  direction in air and is focused by a lens of NA = 0.9. The generation of the longitudinal electric field perpendicular to the focal plane in Fig. 3 will have a very large impact on the excitation of chiral particles, especially the measurement of single particles. As shown in Fig. 3(f), when the particle is off axis, the  $z$  component of the electric field will have an increasing impact on the particle, which is of great concern to us. In order to facilitate the exploration of the chirality at the electric dipole resonance, we select dipolar resonance wavelength 1320 nm and substitute it into the offset factor to explore the optical activity of the structure in a tightly focused light field.

First, we present the spectra of the gold helicoids and helix excited by tightly focused and plane-wave circularly polarized light in air. Here, CD can be calculated as the difference in absorption as  $\text{CD} = A_{\text{LCP}} - A_{\text{RCP}}$ , and circular differential scattering (CDS) [25] is known as  $\text{CDS} = S_{\text{LCP}} - S_{\text{RCP}}$ . Experimentally, it is easier to measure the scattering spectrum of a single particle than the absorption spectrum, so in this study we mainly discuss the scattering differences of particles under the incidence of circularly polarized light.

Figure 4 shows the scattering spectra of a single right-handed nanohelix excited by circularly polarized plane waves and tightly focused light. There are obvious resonances at 600, 760, and 1320 nm, corresponding to electric quadrupole resonance (600 nm) and dipole resonances (760 and 1320 nm). From Figs. 4(a) and 4(b), we can see that when the helix is at the focal point of the object plane of the objective lens, the scattering spectrum obtained by the tightly focused excitation is almost the same as that excited by the plane wave, except for a slight change in the intensity of the high-order resonance. This is due to the fact that the center of the focusing field is dominated by the transverse electric field, and the longitudinal electric field in the  $z$  direction is almost zero. Figures 4(c) and 4(d) show the scattering spectra of the nanohelix at 300 and 400 nm out of focus in the  $x$  direction, where we can see a clear chiral signal inversion at the resonance wavelength 1320 nm. An inverse chiral response is also found at the higher-order resonance (550 nm). Through numerical calculations, we find that the position of the particles in the tightly focused light field has a significant impact on the final experimental results. Next, we will analyze the reasons for the inversion of chiral signals through multipolar decomposition.

Figure 5(a) shows that the resonances at 760 and 1320 nm are both dominated by dipole resonance, and the higher-order resonance at 550 nm is contributed by the electric dipole and quadrupole moments. It can be seen from the Cartesian component of the electric dipole moment in Fig. 5(b) that although there is no electric field in the  $z$  direction under plane-wave irradiation, the resonance at 1320 nm is dominated by the  $z$  component of the electric dipole moment, which can be attributed to its special geometry. When the helix deviates from the center of the tightly focused light field, the  $z$ -direction electric field of the tightly focused light field has a

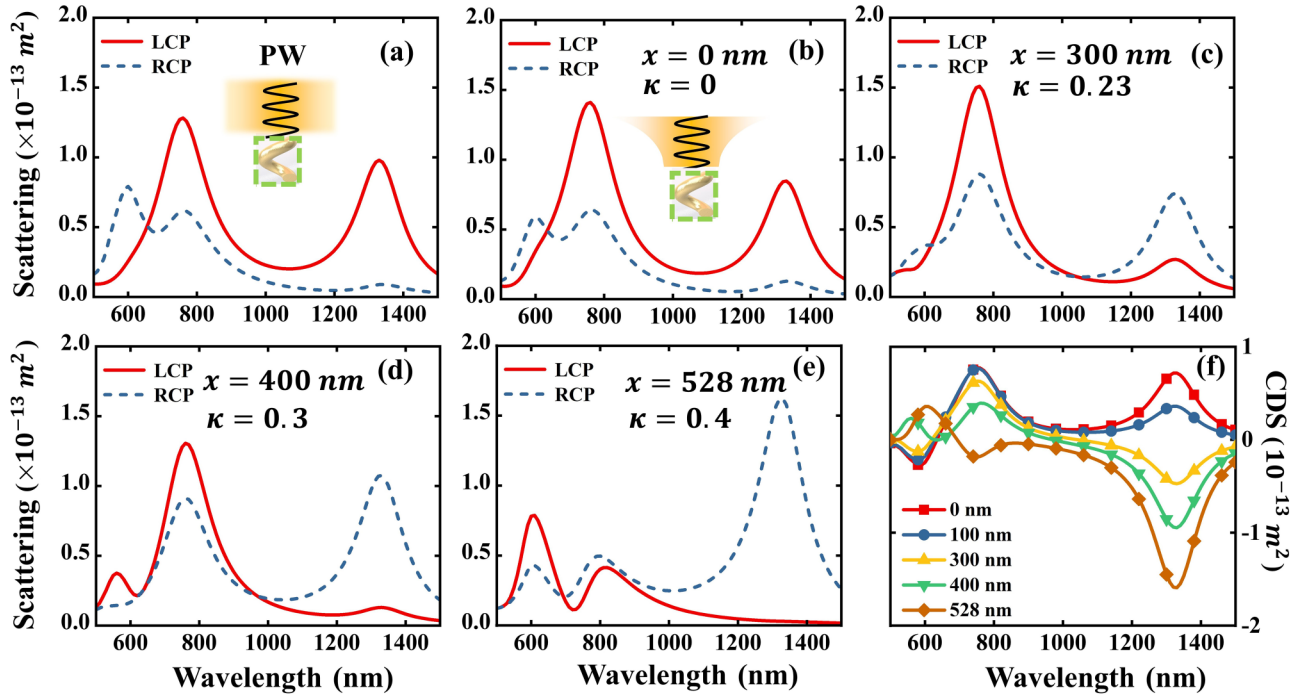


FIG. 4. Scattering spectra of nanohelix under excitation with plane waves and tightly focused light. (a) Scattering spectrum of nanohelix under plane waves. (b–e) Scattering spectra of the helix at different locations in the tightly focused field. (f) CDS spectra of the helix at different positions.

greater impact on the helix, and even causes chirality reversal at 1320 and 550 nm [Figure 5(c)]. As shown in Fig. 5(d), the  $y$  and  $z$  components of the electric dipole moment of the helix in the tightly focused circularly polarized light field are reversed, ultimately leading to the reversal of chirality at the wavelength. The surface charge distributions in Figs. 5(e) and 5(f) also show that the charge appears to oscillate mainly in the  $z$  direction at this resonance. When the nanohelix is irradiated by plane waves, LCP stimulates a stronger  $z$ -direction electric dipole moment; while under tightly focused incidence, RCP stimulates a stronger  $z$ -direction electric dipole moment. Although the light intensity far from the center of the light field is much weaker than the center of the light field, resulting in a weak surface charge distribution, chiral inversion still has a non-negligible impact on actual measurements. In addition, we also calculate the optical response of symmetric silver heterodimers under excitation of the plane wave and tightly focused light field in Fig. 9 of Appendix A. The dimer only exhibits chiral response under tilted excitation with a plane wave, which is known as extrinsic chirality. However, with tightly focused light, the dimer shows chiral response when the optical axis is not tilted but the dimer is off optical axis. As shown in Fig. 8, we find a clear difference between plane-wave excitation and tightly focused light excitation when the particle is off axis. The heterodimer at the focal position does not exhibit a chiral response, but as the extrinsic chiral structure is positioned further away from the focal point, its chiral response increases with increasing offset. Higher-order resonances are more easily excited under tightly focused light fields and become increasingly stronger with increasing offset, thus exciting the higher-order chirality. This is because after the incident light is focused by the objective lens, the

electric field component is deflected, exciting extrinsic chirality. The incidence of a tightly focused light field is equivalent to the superposition of plane waves in the far-field region with angles of incidence from 0 to  $\theta$ . The particle is excited by a symmetric electric field distribution at the focus, but the off-axis electric field is no longer symmetric. The electric field components of obliquely incident light can excite higher-order resonances and generate extrinsic chirality.

#### IV. EXPERIMENT

Currently, most theoretical studies exploring plasmon chirality perform calculations with plane-wave incidence. However, the high-NA objectives are often utilized in actual measurements, resulting in an underestimate of the CD of structures that are easily excited in the longitudinal direction. For the experimental demonstration of the proposed scheme, we choose the chiral nanohelicoids to measure the position dependence of its optical response. We synthesized chiral gold nanohelicoids using the method in Appendix B and dropped the dilute solution on an ITO quartz glass substrate. Next, we measure the reflection spectra of chiral nanohelicoids at different positions of a tightly focused circularly polarized light field to explore the effect of position on the chiral response. Our setup is schematically depicted in Fig. 6(a). First, we prepare a continuous white-light laser beam in free space. The beam is expanded by a beam expander composed of two objective lenses, and then passes through a wide-spectrum polarizing prism (GTH10M, Thorlabs), and broadband half-wave (FR600HM, Thorlabs) and quarter-wave (FR600QM, Thorlabs) fresnel rhomb retarders to generate and switch the circular polarization state of the incident light. The expanded

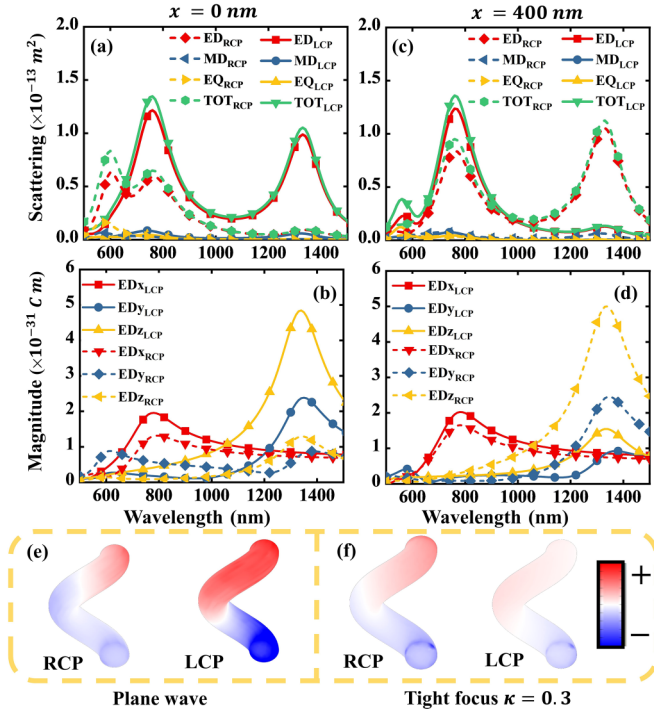


FIG. 5. Multipolar scattering spectra of a nanohelix under plane waves and tightly focused circularly polarized light excitation. (a) Scattering cross section of multipole moments under plane waves. (b) The magnitude of the dipole moment component under plane waves. (c), (d) Multipolar scattering of a nanohelix at 400 nm away from the center of a tightly focused circularly polarized light field and the magnitude of the dipole moment component. (e), (f) The surface charge distribution of a nanohelix at the 1320 nm resonance under a plane wave and tightly focused light field.

circularly polarized beam is focused by an immersion-type microscope objective with a NA of 1.3. The field impinges a sample consisting of chiral gold cubic nanoparticles (side length approximately 100 nm) attached to a quartz glass substrate ( $n = 1.51$ ). Since oil can reduce the reflection of the light beam shining on the glass interface, thereby reducing the interference of reflected light on our measurements, we use an immersion-type microscope objective to measure the spectrum of particles. The position of the particles is precisely controlled by a piezoelectric ceramic displacement platform. Since both the particles and the light spot are very small, we move the position of the particles with a step size of 50 nm, so that the particles pass along the diameter of the light spot and record the reflection spectra at different positions, as shown in Fig. 6(b). In the experiment, we can observe that when the particles are in different positions of the light spot, the color of their scattering will change significantly. We measure the reflectance spectra of a single nanohelicoid [Figure 6(c)] and normalize them with the reflectance spectra of spots without particles (there is still slight interfacial reflection despite oil being applied).

Figures 6(d) and 6(e) show the reflection spectra of the particle slowly sweeping across the light spot of different circularly polarized light. The reflection spectrum changes significantly with the movement of the nanohelicoids. As the nanohelicoids pass through the focus of the light field, the

CDS also undergoes an obvious chirality reversal, as shown in Fig. 6(f). We also performed numerical calculations of the optical response of nanohelices in oil in a tightly focused light circularly polarized field, as shown in Figs. 6(g)–6(i). It can also be seen that as the nanohelicoid approaches the center of the light field, its scattering cross section gradually increases, reaching a maximum at the center. CDS will be reversed as the particle moves through the center of the light field. Due to the difference between the experimentally measured and simulated structures [37,38], the simulated CDS is smaller than the experimental one, but the chirality reversal in the simulation still verifies the correctness of our experiment. With the simulations, we attribute the changes in CDS to the strong focusing of the light field. The incident circularly polarized light will be deflected after being focused by a high numerical aperture objective lens, causing the light field that deviates from the focus to become elliptically polarized light with a longitudinal electric field component  $E_z$  [Figs. 3(a) and 3(d)]. As shown in Fig. 10 of Appendix A, the opposite electric field components on the left and right sides of the focus will excite different electric displacements of the chiral particle, resulting in asymmetric chiral responses and chirality reversal on the left and right sides of the focus. This is also probably the reason that the CD spectra are not stable for the same particle during serial measurements in a lot of experiments.

## V. CONCLUSION

In this paper, we have investigated the position dependence of the chiral response of chiral metamolecules under excitation with tightly focused circularly polarized light. Utilizing a chiral nanohelix and nanohelicoids that exhibit great CD, we explored their optical activity at different positions in the focused light field. When the nanoparticle is located at the focal axis of a tightly focused light field, the chiral signal of the dipole resonance is almost consistent with a plane wave since the  $z$ -component electric field is nearly zero at the center. The electric quadrupole resonance changes slightly, which is attributed to the change of the electric field gradient under tight focusing. When the particles are off axis, the electric field in the  $z$ -axis direction induces the generation of an electric dipole moment in the  $z$  direction. As the offset increases, the opposite circular dichroism induced by the  $z$  component can be obtained. We also describe the chiral response when extrinsic chiral structures are moved out of the optical axis. Chiral responses of off-axis symmetric structures can also be excited and are extremely pronounced at higher-order resonances. To verify our results, we measured the reflection spectra of the chiral nanohelicoids at different positions in a tightly focused circularly polarized light field. The reflection spectrum of the nanohelicoids changes significantly as the position of the particles passes through the focus of the light field, and the CDS is also reversed. This phenomenon has rarely been explored quantitatively before, but the measurement of single chiral particles is extremely important. In conclusion, we have theoretically and experimentally explored the optical activity of chiral particles in tightly focused circularly polarized light fields, which can provide a more accurate reference for the measurement of chirality and the exploration of the mechanism of chiral metamolecules.

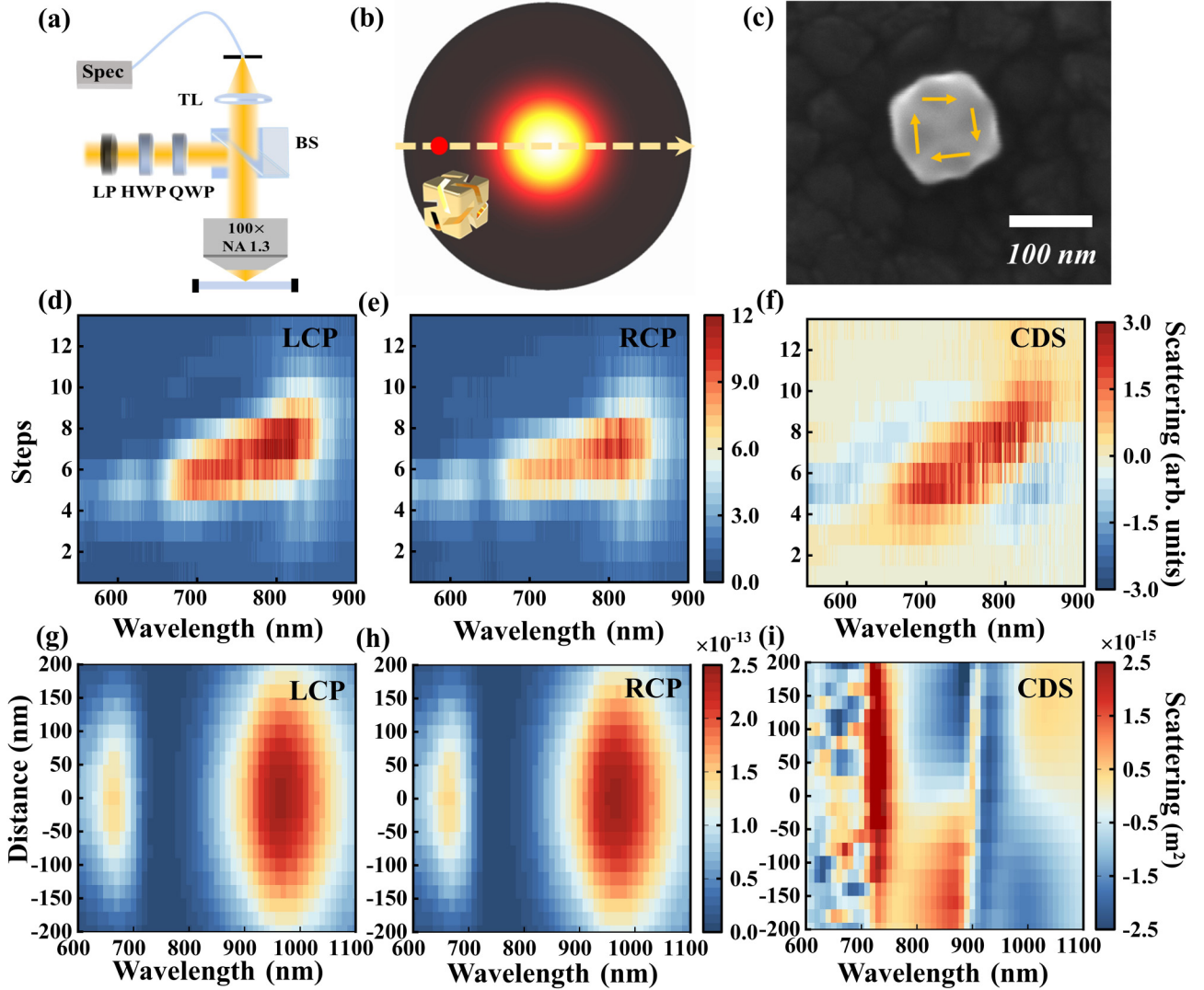


FIG. 6. Experimental measurements of single plasmonic nanohelicoids under tightly focused circularly polarized light excitation. (a) The device for single-particle reflectance spectrum measurement. (b) Schematic diagram of particles passing through a tightly focused light spot. (c) Scanning electron microscope image of chiral nanohelicoids. (d)–(f) Experimental reflection and CDS spectra of nanohelicoids at different positions when passing through the light spot in steps of 50 nm. (g)–(i) Calculated scattering cross section and CDS spectra of nanohelicoids at different positions.

**ACKNOWLEDGMENT**

The authors acknowledge the financial support of this work from the National Natural Science Foundation of China (NSFC) (Grants No. 12074054, No. 12274054, and No. 12204085).

**APPENDIX A: DETAILS AND SUPPORTING RESULTS OF THE SIMULATION**

The spectra of the chiral structures were calculated by the commercial finite element software COMSOL. The scattering field method in COMSOL is applied to calculate the optical response of the chiral nanoparticles, and the background field is given by Eq. (3) derived from the angular spectrum. The plasmonic gold nanohelix and nanorices dimer was placed in the air ( $n = 1$ ), and the dielectric functions of gold and silver were obtained from Ref. [32]. For comparison with

experiments, nanohelicoids were placed in oil ( $n = 1.51$ ) for calculations. The nanohelix was created by the geometry that comes with COMSOL. The major radius is 60 nm, its minor radius is 35 nm, and its axial radius and radial radius are 230 and 0 nm, respectively. The side length of the nanohelicoids in Fig. 7(b) is 120 nm, the width of the incision is 18 nm, and the depth is 37 nm. The larger nanorice in Fig. 7(c) has a major axis radius of 140 nm and a minor axis of 33 nm, and the smaller nanorice has a major axis radius of 95 nm and a minor axis of 21 nm. All meshes in the simulation are smaller than one-sixth of the incident wavelength (500 nm).

The wavelength-dependent scattering spectrum was obtained by dividing the scattering power by the light intensity:  $\sigma_{\text{scat}} = P_{\text{scat}}/I_0$ , where  $P_{\text{scat}}$  is the scattering power integrated by the Poynting vector on the inner interface of a perfectly matched layer (PML), and the  $I_0 = \frac{n}{2Z_0} |E_{\text{inc}}|^2$  is the incident electric field intensity. Compared with the case of plane-wave

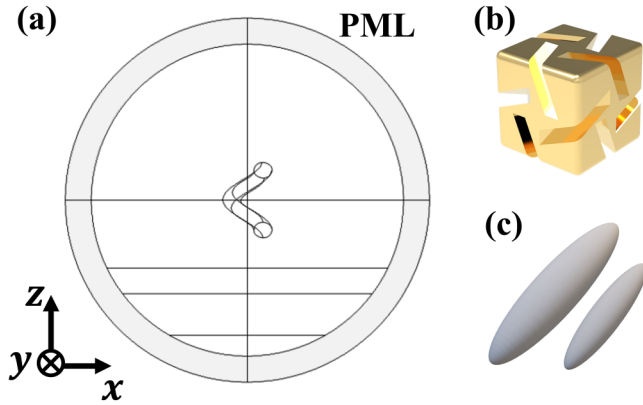


FIG. 7. Schematic illustration of simulated structures such as nanohelix, nanohelicoids, and nanorices dimer. The Cartesian coordinates of the system are shown in the inset.

incidence, the electric field intensity in the tightly focused light field exhibits a Gaussian distribution (Fig. 8). Moreover, the increase in the wavelength of incident light causes the diameter of the focused spot to gradually increase, accompanied by a change in intensity distribution. Typically,  $E_{inc}$  is the incident electric field at the center of mass of the structure. Therefore, in simulations of nanohelix and nanorice dimers, we normalize the scattering power by the electric field at the center of mass of the particle to obtain the scattering cross section. However, in the experiment, we can only measure the spectrum of the entire light spot but cannot measure the spectrum of the electric field where the particles are located. In order to compare with the experiment, we averaged the  $|E_{inc}|^2$

on the plane of  $z = 0$  nm and then substituted it into  $I_0$  in the simulation of nanohelicoids. To be consistent with the experimental conditions, the scattered power  $P_{scat}$  of nanohelicoids is obtained by integrating over a semicircle corresponding to the numerical aperture 1.3. In addition, we have presented the scattering and CDS spectra of the silver dimer, along with the corresponding electric field vectors and Poynting vectors for tightly focused circularly polarized light, see Figs. 9 and 10.

## APPENDIX B: SYNTHESIS OF NANOHELICIDS

The chiral nanoparticles were prepared by a two-step seeded growth method proposed by Lee *et al.* [37,39]. Firstly, Au seeds were prepared by the rapid reduction of  $Au^{3+}$  in the solution. We mixed 7.5 ml of cetyltrimethylammonium bromide (CTAB, 100 mM) and 0.25 ml of  $HAuCl_4$  (10 mM) aqueous solutions, and then rapidly injected 0.8 ml of  $NaBH_4$  (10 mM). The solution instantly changed to brown, indicating the generation of small Au seeds. The solution containing Au seeds was kept at 30 °C for 3 h, and diluted (1:10) in de-ionized water.

The first-step seeded growth that generates Au nanocubes proceeded via successively injecting 1.6 ml of CTAB (100 mM), 0.2 ml of  $HAuCl_4$  (10 mM), and 0.95 ml of L-ascorbic acid (AA, 100 mM) aqueous solutions, and 5  $\mu$ l diluted seeds into 8 ml de-ionized water. After thoroughly mixing the solution, Au nanocubes grew in the following 15 min without disturbing the solution. The Au nanocubes were washed twice and redispersed in CTAB (1 mM) solution.

The second-step growth uses the Au nanocubes as the seeds to synthesize the chiral nanoparticles. The growth solution was prepared by adding 0.8 ml of CTAB (100 mM)

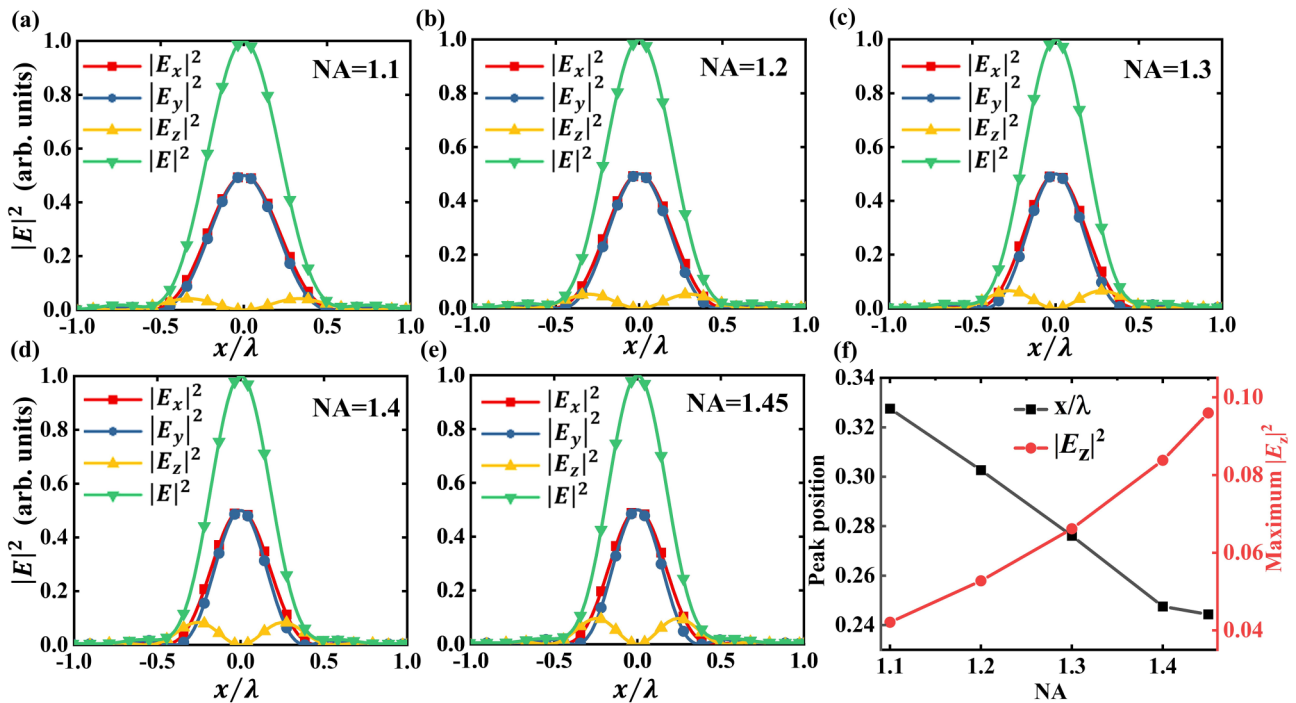


FIG. 8. Electric energy density of circularly polarized light focused by objective lenses with different numerical apertures. (a)–(e) Normalized electric field components of tightly focused circularly polarized light with different NA. (f) The trend of the maximum value of  $|E_z|^2$  and its peak position with NA.

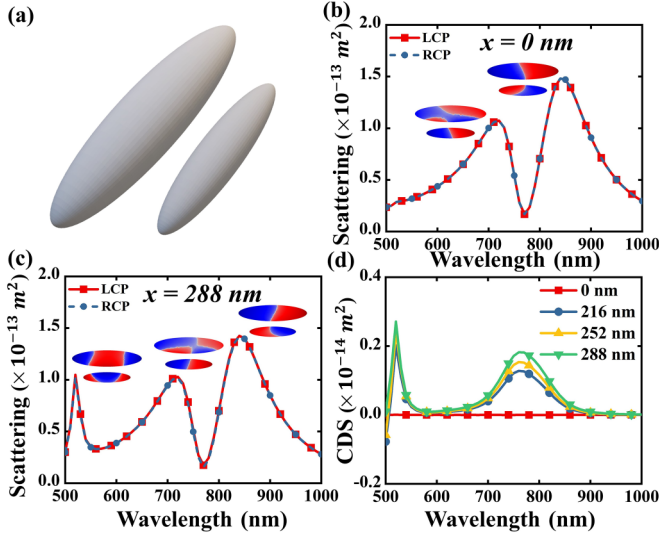


FIG. 9. Scattering and CDS spectra of silver heterodimers excited by tightly focused circularly polarized light. (a) Schematic structural diagram of silver heterodimer. (b), (c) Scattering of silver heterodimers at different offset positions in tightly focused circularly polarized light fields. (d) CDS of silver heterodimers at different offsets. The insets in (b), (c) are the surface charge distributions of the heterodimer at the resonance wavelength.

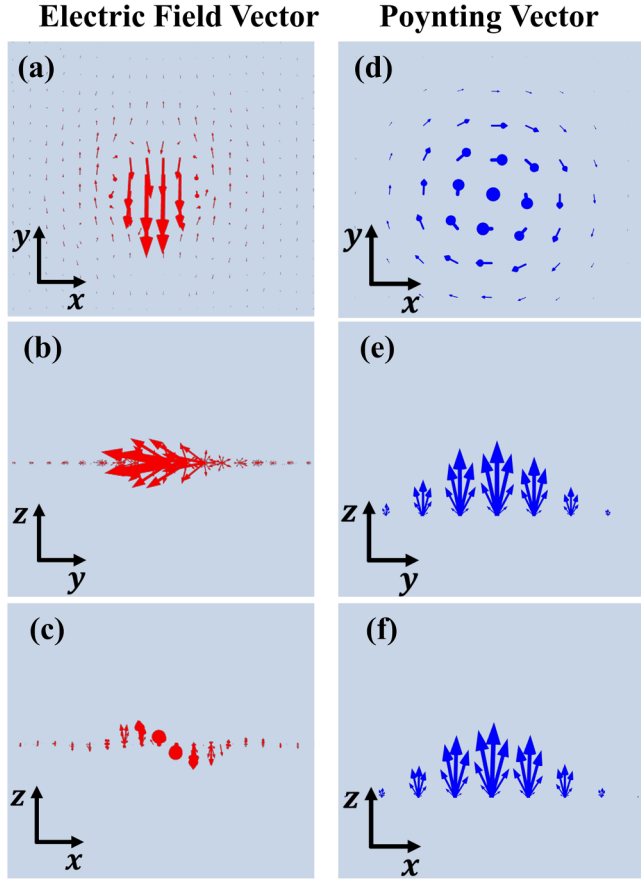


FIG. 10. Schematic of the electric field vector (a)–(c) and Poynting vector (d)–(f) for circularly polarized light tightly focused on the plane  $z = 0 \text{ nm}$ .

and 0.1 ml of  $\text{HAuCl}_4$  (10 mM) aqueous solutions into 3.95 ml de-ionized water, followed by a rapid injection of 0.475 ml AA (100 mM) aqueous solution. To initiate the growth, 10  $\mu\text{l}$  of L-cysteine hydrochloride monohydrate aqueous solution and 50  $\mu\text{l}$  of Au nanocube seeds were successively injected into the growth solution. During the 1 h growth at 30  $^\circ\text{C}$ , the solution gradually turned from pink to blue, indicating the formation of larger particles with stronger scattering. The resultant nanoparticles were washed twice, and then were redispersed in CTAB (1 mM) solution.

### APPENDIX C: MULTIPOLAR DECOMPOSITION

The induced polarization density  $\mathbf{P}_\omega$  calculated by COMSOL is extracted to determine the spectral multipolar response [40].

$$p_\alpha = - \left\{ \int d^3 \mathbf{r} P_\alpha^\omega j_0(kr) + \frac{k^2}{2} \int d^3 \mathbf{r} [3(\mathbf{r} \cdot \mathbf{P}_\omega) r_\alpha - r^2 P_\alpha^\omega] \frac{j_2(kr)}{(kr)^2} \right\}, \quad (\text{C1})$$

$$m_\alpha = \frac{3i\omega}{2} \int d^3 \mathbf{r} (\mathbf{r} \times \mathbf{P}_\omega)_\alpha \frac{j_1(kr)}{kr}, \quad (\text{C2})$$

$$Q_{\alpha\beta}^e = -3 \left\{ \int d^3 \mathbf{r} [3(r_\beta P_\alpha^\omega + r_\alpha P_\beta^\omega) - 2(\mathbf{r} \cdot \mathbf{P}_\omega) \delta_{\alpha\beta}] \frac{j_1(kr)}{kr} + 2k^2 \int d^3 \mathbf{r} [5r_\alpha r_\beta (\mathbf{r} \cdot \mathbf{P}_\omega) - (r_\alpha P_\beta + r_\beta P_\alpha) r^2 - r^2 (\mathbf{r} \cdot \mathbf{P}_\omega) \delta_{\alpha\beta}] \frac{j_3(kr)}{(kr)^3} \right\}, \quad (\text{C3})$$

$$Q_{\alpha\beta}^m = 15i\omega \int d^3 \mathbf{r} \{ r_\alpha (\mathbf{r} \times \mathbf{P}_\omega)_\beta + r_\beta (\mathbf{r} \times \mathbf{P}_\omega)_\alpha \} \frac{j_2(kr)}{(kr)^2}, \quad (\text{C4})$$

where  $p$ ,  $m$ , and  $Q$  are the electric dipole and magnetic dipole moment, electric quadrupole, and magnetic quadrupole

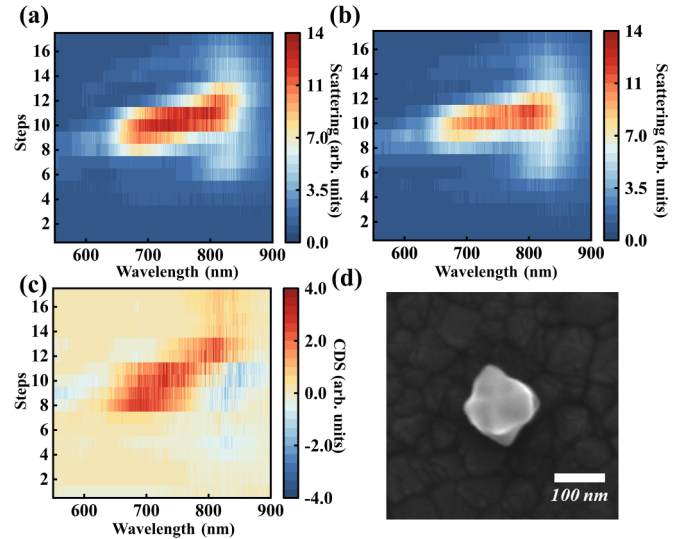


FIG. 11. Experimental measurements of single plasmonic nanohelicoids under tightly focused circularly polarized light excitation.



moment. The subscripts  $\alpha$ ,  $\beta = x, y, z$  represent the coordinate components of the multipole moment.  $\mathbf{r} = (x, y, z)$ ,  $k$  is the wave vector of the incident light, and the contribution of the multipole moment to the total scattering cross section can be easily obtained.

$$C_{\text{scat}} = C_{\text{scat}}^p + C_{\text{scat}}^m + C_{\text{scat}}^{\mathcal{Q}^e} + C_{\text{scat}}^{\mathcal{Q}^m} + \dots$$

$$= \frac{k^4}{6\pi\epsilon_0^2 |\mathbf{E}_{\text{inc}}|^2} \left[ \sum_{\alpha} \left( |p_{\alpha}|^2 + \frac{|m_{\alpha}|^2}{c} \right) \right]$$

$$+ \frac{1}{120} \sum_{\alpha\beta} \left( |kQ_{\alpha\beta}^e|^2 + \left| \frac{kQ_{\alpha\beta}^m}{c} \right|^2 \right) + \dots \quad (\text{C5})$$

#### APPENDIX D: REPLICATION OF EXPERIMENTS

We also measured the scattering spectra of multiple particles. The experimental data showed that the experiment was reproducible and the main conclusions were valid (Fig. 11).

- 
- [1] L. D. Barron, *Molecular Light Scattering and Optical Activity*, 2nd ed. (Cambridge University Press, Cambridge, 2004).
- [2] A. Kuzyk, M. J. Urban, A. Idili, F. Ricci, and N. Liu, Selective control of reconfigurable chiral plasmonic metamolecules, *Sci. Adv.* **3**, e1602803 (2017).
- [3] Y. Liu, L. Ma, S. Jiang, C. Han, P. Tang, H. Yang, X. Duan, N. Liu, H. Yan, and X. Lan, DNA programmable self-assembly of planar, thin-layered chiral nanoparticle superstructures with complex two-dimensional patterns, *ACS Nano* **15**, 16664 (2021).
- [4] Y. Hou, M. Qiu, Z. Cao, J. Zhou, H. C. Ong, W. Jin, J. Du, and D. Lei, High- $Q$  circular dichroism resonances in plasmonic lattices with chiral unit cells, *Adv. Funct. Mater.* **32**, 2204095 (2022).
- [5] Y. Hou, H. M. Leung, C. T. Chan, J. Du, H. L.-W. Chan, and D. Y. Lei, Ultrabroadband optical superchirality in a 3D stacked-patch plasmonic metamaterial designed by two-step glancing angle deposition, *Adv. Funct. Mater.* **26**, 7807 (2016).
- [6] Y. Gorodetski, A. Drezet, C. Genet, and T. W. Ebbesen, Generating far-field orbital angular momenta from near-field optical chirality, *Phys. Rev. Lett.* **110**, 203906 (2013).
- [7] G. Zheng, J. He, V. Kumar, S. Wang, I. Pastoriza-Santos, J. Perez-Juste, L. M. Liz-Marzan, and K. Y. Wong, Discrete metal nanoparticles with plasmonic chirality, *Chem. Soc. Rev.* **50**, 3738 (2021).
- [8] J. K. Gansel, M. Thiel, M. S. Rill, M. Decker, K. Bade, V. Saile, G. Von Freymann, S. Linden, and M. Wegener, Gold helix photonic metamaterial as broadband circular polarizer, *Science* **325**, 1513 (2009).
- [9] C. Xu, Z. Ren, H. Zhou, J. Zhou, C. P. Ho, N. Wang, and C. Lee, Expanding chiral metamaterials for retrieving fingerprints via vibrational circular dichroism, *Light: Sci. Appl.* **12**, 154 (2023).
- [10] R. M. Kim, J.-H. Huh, S. Yoo, T. G. Kim, C. Kim, H. Kim, J. H. Han, N. H. Cho, Y.-C. Lim, S. W. Im, E. Im, J. R. Jeong, M. H. Lee, T.-Y. Yoon, H.-Y. Lee, Q. H. Park, S. Lee, and K. T. Nam, Enantioselective sensing by collective circular dichroism, *Nature (London)* **612**, 470 (2022).
- [11] Y. Zhao, A. N. Askarpour, L. Sun, J. Shi, X. Li, and A. Alu, Chirality detection of enantiomers using twisted optical metamaterials, *Nat. Commun.* **8**, 14180 (2017).
- [12] E. Hendry, T. Carpy, J. Johnston, M. Popland, R. V. Mikhaylovskiy, A. J. Laphorn, S. M. Kelly, L. D. Barron, N. Gadegaard, and M. Kadodwala, Ultrasensitive detection and characterization of biomolecules using superchiral fields, *Nat. Nanotechnol.* **5**, 783 (2010).
- [13] E. Hendry, R. V. Mikhaylovskiy, L. D. Barron, M. Kadodwala, and T. J. Davis, Chiral electromagnetic fields generated by arrays of nanoslits, *Nano Lett.* **12**, 3640 (2012).
- [14] R. Tullius, A. S. Karimullah, M. Rodier, B. Fitzpatrick, N. Gadegaard, L. D. Barron, V. M. Rotello, G. Cooke, A. Laphorn, and M. Kadodwala, "Superchiral" spectroscopy: Detection of protein higher order hierarchical structure with chiral plasmonic nanostructures, *J. Am. Chem. Soc.* **137**, 8380 (2015).
- [15] R. Tullius, G. W. Platt, L. Khosravi Khorashad, N. Gadegaard, A. J. Laphorn, V. M. Rotello, G. Cooke, L. D. Barron, A. O. Govorov, A. S. Karimullah, and M. Kadodwala, Superchiral plasmonic phase sensitivity for fingerprinting of protein interface structure, *ACS Nano* **11**, 12049 (2017).
- [16] Y. Tang and A. E. Cohen, Optical chirality and its interaction with matter, *Phys. Rev. Lett.* **104**, 163901 (2010).
- [17] Y. Tang and A. E. Cohen, Enhanced enantioselectivity in excitation of chiral molecules by superchiral light, *Science* **332**, 333 (2011).
- [18] J. Kumar, H. Eraña, E. López-Martínez, N. Claes, V. F. Martín, D. M. Solís, S. Bals, A. L. Cortajarena, J. Castilla, and L. M. Liz-Marzán, Detection of amyloid fibrils in Parkinson's disease using plasmonic chirality, *Proc. Natl. Acad. Sci. USA* **115**, 3225 (2018).
- [19] L. Xu, X. Wang, W. Wang, M. Sun, W. J. Choi, J.-Y. Kim, C. Hao, S. Li, A. Qu, M. Lu, X. Wu, F. M. Colombari, W. R. Gomes, A. L. Blanco, A. F. de Moura, X. Guo, H. Kuang, N. A. Kotov, and C. Xu, Enantiomer-dependent immunological response to chiral nanoparticles, *Nature (London)* **601**, 366 (2022).
- [20] M. Matuschek, D. P. Singh, H. H. Jeong, M. Nesterov, T. Weiss, P. Fischer, F. Neubrech, and N. Liu, Chiral plasmonic hydrogen sensors, *Small* **14**, 1702990 (2017).
- [21] M. Qiu, L. Zhang, Z. Tang, W. Jin, C.-W. Qiu, and D. Y. Lei, 3D metaphotonic nanostructures with intrinsic chirality, *Adv. Funct. Mater.* **28**, 1803147 (2018).
- [22] P. Wozniak, I. De Leon, K. Hofflich, C. Haverkamp, S. Christiansen, G. Leuchs, and P. Banzer, Chiroptical response of a single plasmonic nanohelix, *Opt. Express* **26**, 19275 (2018).
- [23] P. Banzer, P. Wozniak, U. Mick, I. De Leon, and R. W. Boyd, Chiral optical response of planar and symmetric nanotrimers enabled by heteromaterial selection, *Nat. Commun.* **7**, 13117 (2016).
- [24] S. Nechayev, P. Wozniak, M. Neugebauer, R. Barczyk, and P. Banzer, Chirality of symmetric resonant heterostructures, *Laser Photonics Rev.* **12**, 1800109 (2018).
- [25] C. Bustamante, I. Tinoco, and M. F. Maestre, Circular differential scattering can be an important part of the circular-dichroism

- of macromolecules, *Proc. Natl. Acad. Sci. USA* **80**, 3568 (1983).
- [26] P. Stachelek, L. MacKenzie, D. Parker, and R. Pal, Circularly polarised luminescence laser scanning confocal microscopy to study live cell chiral molecular interactions, *Nat. Commun.* **13**, 553 (2022).
- [27] L. Novotny and B. Hecht, *Principles of Nano-Optics*, 2nd ed. (Cambridge University Press, Cambridge, 2012).
- [28] E. Wolf, Electromagnetic diffraction in optical systems—I. An integral representation of the image field, *Proc. R. Soc. London, Ser. A* **253**, 349 (1997).
- [29] B. Richards and E. Wolf, Electromagnetic diffraction in optical systems—II. Structure of the image field in an aplanatic system, *Proc. R. Soc. London, Ser. A* **253**, 358 (1997).
- [30] L.-Y. Wang, K. W. Smith, S. Dominguez-Medina, N. Moody, J. M. Olson, H. Zhang, W.-S. Chang, N. Kotov, and S. Link, Circular differential scattering of single chiral self-assembled gold nanorod dimers, *ACS Photonics* **2**, 1602 (2015).
- [31] K. W. Smith, H. Zhao, H. Zhang, A. Sánchez-Iglesias, M. Grzelczak, Y. Wang, W.-S. Chang, P. Nordlander, L. M. Liz-Marzán, and S. Link, Chiral and achiral nanodumbbell dimers: The effect of geometry on plasmonic properties, *ACS Nano* **10**, 6180 (2016).
- [32] P. B. Johnson and R. W. Christy, Optical constants of the noble metals, *Phys. Rev. B* **6**, 4370 (1972).
- [33] G. Zhu, Z. Sun, J. Liu, and Y. Fang, Multipole analysis of the extinction cross section and circular dichroism of chiral meta-molecules with optical theorem, *Adv. Opt. Mater.* **11**, 2202677 (2023).
- [34] G. Zhu, H. Wei, Z. Sun, J. Liu, X. Wei, Y. Liang, W. Peng, and Y. Fang, Quantitative analysis of circular dichroism at higher-order resonance of extrinsic plasmonic chiral nanostructures using multipole decomposition combined with the optical theorem, *New J. Phys.* **25**, 103044 (2023).
- [35] L. Hu, Y. Huang, L. Fang, G. Chen, H. Wei, and Y. Fang, Fano resonance assisting plasmonic circular dichroism from nanorice heterodimers for extrinsic chirality, *Sci. Rep.* **5**, 16069 (2015).
- [36] X. Tian, Y. Fang, and B. Zhang, Multipolar Fano resonances and Fano-assisted optical activity in silver nanorice heterodimers, *ACS Photonics* **1**, 1156 (2014).
- [37] H.-E. Lee, H.-Y. Ahn, J. Mun, Y. Y. Lee, M. Kim, N. H. Cho, K. Chang, W. S. Kim, J. Rho, and K. T. Nam, Amino-acid- and peptide-directed synthesis of chiral plasmonic gold nanoparticles, *Nature (London)* **556**, 360 (2018).
- [38] Y. Chen, J. Zheng, L. Zhang, S. Li, Y. Chen, K. K. Chui, W. Zhang, L. Shao, and J. Wang, Inversion of the chiroptical responses of chiral gold nanoparticles with a gold film, *ACS Nano* **18**, 383 (2023).
- [39] H.-Y. Ahn, H.-E. Lee, K. Jin, and K. T. Nam, Extended gold nano-morphology diagram: Synthesis of rhombic dodecahedra using CTAB and ascorbic acid, *J. Mater. Chem. C* **1**, 6861 (2013).
- [40] R. Alaei, C. Rockstuhl, and I. Fernandez-Corbaton, An electromagnetic multipole expansion beyond the long-wavelength approximation, *Opt. Commun.* **407**, 17 (2018).